Numerical investigation into the vulnerability to liquefaction of an embedded pipeline exposed to ocean storms

H-Y Zhao[a*], X-L Liu[b], D-S Jeng[c], J-H Zheng[a], J-S Zhang[a], Z-D Liang[d]

[a] *State Key Laboratory of Hydrology-Water Resources and Hydraulic Engineering, Hohai University, Nanjing 210098, China*
[b] *Key Laboratory of Marine Environmental Science and Ecology, Ministry of Education, Qingdao 266100, China*
[c] *School of Engineering & Built Environment, Griffith University Gold Coast Campus, Queensland, 4222, Australia*
[d] *School of Civil Engineering, Qingdao University of Technology, Qingdao 266033, China*

Abstract

This paper presents a numerical investigation into the vulnerability to liquefaction of an embedded pipeline exposed to ocean storms. In this study a series of irregular waves similar to a real ocean storm were generated using the JONSWAP spectrum, and their motions with the presence of ocean currents are described using the Reynolds-Averaged Navier-Stokes (RANS) equations. Under storm waves and currents, the dynamics of a seabed with an embedded pipeline were reproduced using a coupled fluid-dynamic framework. An advanced constitutive model (modified Pastor-Zienkiewicz Mark-III) was used to describe the cyclic plasticity of soil. This model was calibrated according to the given soil properties; the predicted results match the wave flume test and geotechnical centrifugal test fairly well when the evolution of residual pore water pressure near the pipe and/or further away are considered. The numerical results indicated that seabed soil is more susceptible to liquefaction due to regular waves than irregular waves. The specific gravity of the pipe can significantly affect the onset and spread of liquefaction in the neighbouring region. As a practical guide, a relationship between the critical wave height and the depth to which the pipe is buried is proposed to control the liquefaction at the bottom of the pipe by selecting feasible backfill materials based on operational requirements and ocean storm conditions.

Keywords: Ocean storm; Pipeline; Cyclic plasticity; Liquefaction; Random wave.

---

[*]Corresponding author.
 Email address: hyzhaohhu@gmail.com (H-Y Zhao[a])

1. Introduction

To design stable subsea pipelines, the potential hazards associated with ocean storms must be taken into consideration, particularly when pipelines are to be embedded in loose silty sand and silt with poor drainage conditions. Under severe environmental loads seabed soils are vulnerable to liquefaction due to cyclic plastic deformation, principal stress axes rotation (PSR), and the build-up of pore water pressure (Sassa and Sekiguchi, 2001; Sumer, 2014). The failure of submarine pipelines caused by storm and wave induced liquefaction has been frequently reported (see for examples, Christian et al. (1974); Herbich et al. (1984)), and without exception every case had enormous environmental impacts and led to huge economic losses. Therefore, a better understanding of the interaction between waves, seabed, and pipelines during an ocean storm is of practical significance.

Recent advances in the field and laboratory studies have accumulated a significant amount of knowledge on the failure mechanism of pipelines buried in loose granular soils that experience accumulating pore-water pressure and progressive liquefaction (Sumer et al., 1999; Jeng, 2001; Teh et al., 2003; Sumer et al., 2006; Damgaard et al., 2006; Luan et al., 2008). However, modelling the complicated interactions between an embedded pipeline and neighbouring residual liquefied soil is formidable. Some researchers adopted Biot's theory framework to simulate the dynamic deformation and water flows that occur in saturated seabed soil around a pipeline. Among these, Zhao et al. (2014) and Zhao and Jeng (2016) developed a simplified quasi-static approach to estimate the progressive nature of liquefaction around an embedded pipeline and a partially backfilled trenched pipeline by using the phase-resolved shear stress to trigger the build-up of residual pore water pressure. However, in these analyses, both oscillatory and residual pore pressure were generated in a decoupled manner while the effect of residual pore pressure on the evolution of oscillatory shear stresses and strains associated with the nonlinear deformation of residual liquefied soil is omitted. Dunn et al. (2006) numerically investigated the interactions between pipeline and seabed using elastoplastic models (Chan, 1995) to capture the cyclic non-linearity of soil due to ocean waves and to predict the pore water pressure that accumulates as a result of the cyclic volumetric contraction of seabed soil. Zhao et al. (2018b) also elucidated the advantage of using elastoplastic models to capture typical soil behaviour in terms of strain softening and cyclic degradation in the course of liquefaction.

The above numerical analyses demonstrated that the appropriate formulation of the cyclic behaviour of marine deposits is the key to modelling pipeline and seabed interactions under wave-induced liquefaction. It has been well-known that ocean waves normally have moveable and periodic characteristics that may produce complex non-proportional and in-situ stress in seabed soil during which the magnitude and direction of principal stress can change in tandem (Cai et al., 2015; Wang et al., 2017b; Zhao et al., 2020). Numerous experimental studies indicate that under continuous rotations of principal stress axes, the rate of increased plastic strain and residual pore water pressure can increase significantly in undrained soil (Ishihara and Towhata, 1983; Towhata and Ishihara, 1985; Wang et al., 2017a). This means that the vulnerability of the seabed to liquefaction may be underestimated if the impact of PSR is ignored. This will then have a detrimental effect on the stability of submarine pipelines. To the best of the authors' knowledge, this fundamental issue has not been addressed for the pipeline design by any existing studies as they relate to the mechanism of wave, seabed, and pipeline interactions. Furthermore, these existing studies only considered regular or periodic wave conditions whereas ocean storms normally consist of a large number of random components with continuous variations in the amplitude of cyclic stress, so the dynamic response of soil may be related to the characteristics of wave grouping in terms of its spectrum (Sassa et al., 2006). To date, there is a lack of investigations into the evolution of pore water pressure and residual liquefaction around a pipeline in the course of storm wave and current loading, although there are some limited field and laboratory data on this problem available in the literature (Sassa et al., 2006; Miyamoto et al., 2020).

Scope and objectives:. This study aims to advance our current knowledge of the mechanism of wave-induced liquefaction around an embedded pipeline during ocean storms. To achieve this, an integrated numerical model has been developed that incorporates the random nature of storm waves, the evolution of storm waves in the presence of currents, the mechanism of coupled flow and deformation in a porous seabed, and the non-linearity of the soil skeleton due to cyclic shearing. In this context, particular attention was paid to implementing an established constitutive model which incorporates the impact of wave-induced principal stress axes rotations (Zhu et al., 2019). The present model is calibrated based on the specified soil properties, whereas the simulated residual pore water pressures are validated against the wave flume

test (Sumer et al., 2006) and geotechnical centrifugal test (Miyamoto et al., 2020). A detailed numerical simulation will then be carried out to study in prototype scale the influence of stress axes rotations, the random nature of storm waves, the presence of ocean currents, and the specific gravity of pipe on the dynamic response of soil to wave-induced liquefaction. Finally, an empirical formulation and graphs for mitigating the instability of pipe due to liquefaction are also proposed for practical engineering design.

2. Description of the numerical model

The present numerical model has two sub-models, a geotechnical model and a hydrodynamic model. A one-way coupling algorithm (Zhao et al., 2018a) is used to allocate a random wave and current loading from the hydrodynamic model to exert pressures onto the geotechnical model as the surface boundary conditions. A brief introduction of each sub-model is given in this section.

2.1. Hydrodynamic model

2.1.1. Navier-Stokes equations

In this hydrodynamic analysis, the evolution of fluid motion is governed by the incompressible Navier-Stokes equations that includes the continuity equation, (1), and the momentum conservation equations, (2).

$$\nabla \cdot \mathbf{u} = 0 \tag{1}$$

$$\frac{\partial \mathbf{u}}{\partial t} + (\mathbf{u} \cdot \nabla) \mathbf{u} = -\frac{1}{\rho_f} \nabla p_d + \mathbf{g} + \frac{1}{\rho_f} \nabla \cdot \tau \tag{2}$$

where $\mathbf{u}$=velocity vector expressed in the Cartesian coordinates; $\mathbf{g}$=the gravitational acceleration; p_d=pseudo-dynamic pressure; ρ_f=fluid density; τ=viscous stress tensor with an Einstein notation of τ_{ij}, for Newtonian fluid that can be given by:

$$\tau_{ij} = \mu \left(\frac{\partial u_i}{\partial x_j} + \frac{\partial u_j}{\partial x_i} \right) \tag{3}$$

where μ denotes the dynamic molecular viscosity for the water and air; u_i and u_j denote the velocity component in the Cartesian system.

2.1.2. Generation of random waves

Following the mathematical representations of Longuet-Higgins (1957), a profile of random sea wave can be interpreted as the superposition of linear components, given by

$$\eta(x,t) = \sum_{i=1}^{\infty} \alpha_i \cos(k_i x - 2\pi \tilde{f}_i t + \varsigma_i) \approx \sum_{i=1}^{M} \cos(k_i x - 2\pi \tilde{f}_i t + \varsigma_i) \tag{4}$$

where M=the number of wave components; α_i=the amplitude of ith wave component; $\tilde{f}_i$=ith mean frequency; ς_i=random initial phase angle which is equally distributed in the range of (0, 2π). In (4), k_i is the wave number of the i-th component which can be determined based on the dispersion relationship given by

$$\left(2\pi \tilde{f}_i\right)^2 = g k_i \tanh k_i d \tag{5}$$

The amplitude of i-th wave component can be determined from a functional frequency spectrum $S(f)$ given by

$$\alpha_i = \sqrt{2S\left(\tilde{f}_i\right) \Delta f_i}, \quad \tilde{f}_i = (f_i + f_{i-1})/2, \quad \Delta f_i = f_i - f_{i-1}. \tag{6}$$

The frequency spectra adopted in this study is the JONSWAP spectrum (Hasselmann et al., 1973). Its mathematical expressions are summarised here.

$$S(f) = \beta_J H_{1/3}^2 T_p^{-4} f^{-5} \exp\left[-1.25\left(T_p f\right)^{-4}\right] \gamma^{\exp\left[-(T_p f - 1)^2/2\sigma^2\right]} \tag{7}$$

$$\beta_J = \frac{0.06238}{0.23 + 0.033\gamma - 0.185(1.9 + \gamma)^{-1}} \times [1.094 - 0.01915 \ln \gamma] \tag{8}$$

$$T_p = \frac{T_{1/3}}{1 - 0.132(\gamma + 0.2)^{-0.559}} \tag{9}$$

$$\sigma = \left\{ \begin{array}{l} \sigma_a : f \le f_p \\ \sigma_b : f \ge f_p \end{array} \right\} \tag{10}$$

where f_p and T_p denote the frequency and corresponding wave period at the spectral peak. In this study the mean value of γ=3.3 that controls the sharpness of the spectral peak is used (Hasselmann et al., 1973).

2.2. Geotechnical model

2.2.1. Coupled fluid-dynamic framework

In this study, the authors used Biot's partially dynamic equations Ulker and Rahman (2009) (also known as "*u-p*" approximations) to describe the mechanism of coupled flow and soil deformation in a saturated porous seabed. The governing equations include the momentum balance of the solid-pore fluid system, (11)– (12), and the continuity equation for the pore fluid, (13), which can be expressed as::

$$\frac{\partial \sigma'_x}{\partial x} + \frac{\partial \tau_{xz}}{\partial z} = -\frac{\partial p}{\partial x} + \rho \frac{\partial^2 u_s}{\partial t^2}, \tag{11}$$

$$\frac{\partial \tau_{xz}}{\partial x} + \frac{\partial \sigma'_z}{\partial z} + \rho g = -\frac{\partial p}{\partial z} + \rho \frac{\partial^2 w_s}{\partial t^2}, \tag{12}$$

$$k\nabla^2 p - \gamma_w n_s \beta_s \frac{\partial p}{\partial t} + k\rho_f \frac{\partial^2 \varepsilon_s}{\partial t^2} = \gamma_w \frac{\partial \varepsilon_s}{\partial t} \tag{13}$$

where p=pore pressure; u_x and u_z=displacement components of soil-solid phase; n=porosity of soil; σ'_x and σ'_z=effective stress components (tension is taken as positive) withstood by the soil skeleton; τ_{xz}=shear stress acting on the soil; g=body acceleration of the porous medium; $\rho = n\rho_f + (1-n)\rho_s$=the averaged density of the saturated medium; k=coefficient of Darcy's permeability which is assumed to be the same in all directions for material with isotropic permeability considered in this study.

In (13), the volumetric strain (ε_s) and compressibility of pore fluid (β_s) are defined as

$$\varepsilon = \frac{\partial u_s}{\partial x} + \frac{\partial w_s}{\partial z}, \quad \beta_s = \frac{1}{K_f} + \frac{1 - S_r}{p_{w0}} \tag{14}$$

where p_{w0}=absolute static pressure; K_f=bulk modulus of the fluid itself which is normally taken as 1.95×10^9 N/m^2 (Yamamoto et al., 1978); and S_r=degree of saturation.

2.2.2. Constitutive model

Based on the theory of generalized plasticity (Pastor et al., 1990), the constitutive relationships between the incremental effective stress $\Delta\sigma'$ and the incremental strain $\Delta\varepsilon$ of the solid-soil phase are defined as,

$$d\sigma'_{ij} = \begin{cases} \left[D^e_{ijkl} - \frac{D^e_{ijmn}m_{mn}n_{st}D^e_{stkl}}{H_L + n_{st}D^e_{stkl}m_{kl}} \right] d\varepsilon_{kl}, & \text{for loading} \\\\ \left[D^e_{ijkl} - \frac{D^e_{ijmn}m_{mn}n_{st}D^e_{stkl}}{H_U + n_{st}D^e_{stkl}m_{kl}} \right] d\varepsilon_{kl}, & \text{for unloading} \end{cases} \tag{15}$$

6

where D^e_{ijkl}=fourth-order tangent elastic stiffness; $H_{L/U}$= plastic modulus at the loading/unloading stage; m_{mn}=plastic flow direction vector; n_{st}=loading or unloading direction vector. Note that in the context of a generalized plasticity, no yield surface or plastic potential have been predefined, whereas the gradients themselves are functions by which the stiffness matrix can be fully described (Pastor et al., 1990).

In this study the authors used the modified Pastor-Zienkiewicz Mark III (PZIII) model (Zhu et al., 2019) so that the impact of principal stress rotation can be considered by relating the model parameters m_{mn}, n_{st}, $H_{L/U}$ to the major principal stress angle ψ. For the loading phase we have

$$H_L = H_0 \cdot p' \cdot \left[1 - \frac{\eta(\psi)}{\eta_f^*}\right]^4 \cdot \left[1 - \frac{q/p'}{M_{g\theta}(\psi)} + \beta_0\beta_1 \exp(-\beta_0\xi)\right], \tag{16}$$

$$m_{ij} = \frac{\frac{\partial g}{\partial \sigma'_{ij}}}{\left\|\frac{\partial g}{\partial \sigma'}\right\|} = \frac{\frac{\partial g}{\partial p'}\frac{\partial p'}{\partial \sigma'_{ij}} + \frac{\partial g}{\partial q}\frac{\partial q}{\partial \sigma'_{ij}} + \frac{\partial g}{\partial \theta}\frac{\partial \theta}{\partial \sigma'_{ij}}}{\left\|\frac{\partial g}{\partial p'}\frac{\partial p'}{\partial \sigma'} + \frac{\partial g}{\partial q}\frac{\partial q}{\partial \sigma'} + \frac{\partial g}{\partial \theta}\frac{\partial \theta}{\partial \sigma'}\right\|}, \tag{17}$$

$$n_{ij} = \frac{\frac{\partial f}{\partial \sigma'_{ij}}}{\left\|\frac{\partial f}{\partial \sigma'}\right\|} + \chi\frac{\partial \psi}{\partial \sigma'_{ij}} = \frac{\frac{\partial f}{\partial p'}\frac{\partial p'}{\partial \sigma'_{ij}} + \frac{\partial f}{\partial q}\frac{\partial q}{\partial \sigma'_{ij}} + \frac{\partial f}{\partial \theta}\frac{\partial \theta}{\partial \sigma'_{ij}}}{\left\|\frac{\partial f}{\partial p'}\frac{\partial p'}{\partial \sigma'} + \frac{\partial f}{\partial q}\frac{\partial q}{\partial \sigma'} + \frac{\partial f}{\partial \theta}\frac{\partial \theta}{\partial \sigma'}\right\|} + \chi\frac{\partial \psi}{\partial \sigma'_{ij}}, \tag{18}$$

$$D^e_{ijkl} = \lambda\delta_{ij}\delta_{kl} + 2G\delta_{ik}\delta_{jl}, \quad G = \frac{G_0 p'}{p'_0}, \quad \lambda = \frac{3K\mu}{1+\mu}, \quad K = \frac{K_{ev0}p'}{p'_0}, \tag{19}$$

where

$$\psi = \frac{1}{2}\tan^{-1}\left[2\tau_{xz}/\left(\sigma'_z - \sigma'_x\right)\right], \tag{20}$$

$$\frac{\partial \psi}{\partial \sigma'_x} = \frac{\tau_{xz}}{\left(\sigma'_x - \sigma'_z\right)^2 + \tau_{xz}^2}, \quad \frac{\partial \psi}{\partial \sigma'_z} = -\frac{\tau_{zx}}{\left(\sigma'_x - \sigma'_z\right)^2 + \tau_{xz}^2},$$

$$\frac{\partial \psi}{\partial \sigma'_y} = 0, \quad \frac{\partial \psi}{\partial \tau_{xz}} = \frac{\left(\sigma'_x - \sigma'_z\right)/2}{\left(\sigma'_x - \sigma'_z\right)^2 + \tau_{xz}^2} = \frac{\partial \psi}{\partial \tau_{zx}}, \tag{21}$$

$$M_{g\theta}(\psi) = M_{g\theta} - U(\psi) \cdot a \cdot M_{g\theta}, \quad \eta(\psi) = \frac{q}{p'} - (1 - U(\psi)) \cdot aM_{g\theta}, \tag{22}$$

$$U(\psi) = \begin{cases} 1 - \cos(2\psi) & 0 \leq \psi \leq \pi/4 \\ 1 - \cos(2|\psi| - \pi) & \pi/4 \leq \psi \leq \pi/2, \end{cases} \tag{23}$$

$$\eta_f^* = \left(M_{f\theta} - aM_{g\theta}\right) \cdot \left(1 + \frac{1}{\alpha_0 + b}\right), \quad \xi = \int |d\xi_q^p|, \tag{24}$$

7

$$\frac{\partial g}{\partial p'} = (1 + \alpha(\psi))\left(M_{g\theta}(\psi) - \frac{q}{p'}\right), \quad \frac{\partial g}{\partial q} = 1, \tag{25}$$

$$\frac{\partial g}{\partial \theta} = -\frac{q}{2M_{g\theta}(\psi)}\left[M_{g\theta}^2 - a \cdot U(\psi) \cdot M_{g\theta}^2\right]\cos 3\theta, \tag{26}$$

$$\frac{\partial f}{\partial p'} = (1 + \alpha(\psi))\left(M_{f\theta}(\psi) - \frac{q}{p'}\right), \quad \frac{\partial f}{\partial q} = 1, \tag{27}$$

$$M_f(\psi) = M_{f\theta} - U(\psi) \cdot a \cdot M_{g\theta}, \tag{28}$$

$$\frac{\partial f}{\partial \theta} = -\frac{q}{2M_{f\theta}(\psi)}\left[M_{f\theta}^2 - a \cdot U(\psi) \cdot M_{g\theta}^2\right]\cos 3\theta, \tag{29}$$

$$M_{g\theta} = \frac{18M_{g0}}{18 + 3(1 + \sin 3\theta)}, \quad M_{f\theta} = \frac{18M_{f0}}{18 + 3(1 + \sin 3\theta)}, \quad \text{and} \tag{30}$$

$$p' = \frac{1}{3}(\sigma_x' + \sigma_y' + \sigma_z'), \tag{31}$$

$$q = \frac{1}{\sqrt{2}}\sqrt{(\sigma_x' - \sigma_y')^2 + (\sigma_x' - \sigma_z')^2 + (\sigma_y' - \sigma_z')^2 + 6\tau_{xz}}. \tag{32}$$

where H_0=parameter that scales the plastic modulus; β_0 and β_1=material constants; G=shear modulus (the initial value is G_0); p_0'=mean effective stress at the end of consolidation phase; δ=Kronecker delta; θ=Lode angle; λ=Lame's constant; K=the bulk modulus (the initial value is K_{ev0}); $\alpha(\psi)$=coefficient related to the stress-dilatancy and the effect of stress axes rotation; χ=the parameter accounting for the impact of principal stress rotation, i.e.,

$$\begin{cases} a = 0, \quad b = 0, \quad \chi = 0 \\ \\ \text{Other cases,} \quad \chi = 1 \end{cases} \tag{33}$$

The formulae for the unloading case are almost identical to the loading case, except for the determination of $\partial g/\partial p'$ and the plastic modulus H_L, which is replaced with H_U, and can be defined as follows:

$$\frac{\partial g}{\partial p'} = -\left|\frac{\partial g}{\partial p'}\right|, \quad H_U = \begin{cases} H_{U0}\left[\frac{M_g(\psi)}{(q/p')_u}\right]^{\gamma_U} & \text{for } \left|\frac{M_g(\psi)}{(q/p')_U}\right| > 1, \\ \\ H_{U0} & \text{for } \left|\frac{M_g(\psi)}{(q/p')_U}\right| \le 1, \end{cases} \tag{34}$$

where H_{U0} and γ_U are model parameters, and $(q/p')_U$ is the effective stress ratio when unloading occurs.

2.2.3. Pipeline model

In this study, the pipeline is considered as an impermeable medium, whereas its deformation is described using Hooke's law. While considering the acceleration of the pipeline in the dynamic analysis, the following equations governing the force equilibrium of the pipeline can be given:

$$G_p\left(\frac{\partial u_p}{\partial x^2} + \frac{\partial u_p}{\partial z^2}\right) + \frac{G_p}{1-2\mu_p}\frac{\partial}{\partial x}\left(\frac{\partial u_p}{\partial x} + \frac{\partial w_p}{\partial z}\right) = \rho_p\frac{\partial^2 u_p}{\partial t^2} \tag{35}$$

$$G_p\left(\frac{\partial w_p}{\partial x^2} + \frac{\partial w_p}{\partial z^2}\right) + \frac{G_p}{1-2\mu_p}\frac{\partial}{\partial x}\left(\frac{\partial u_p}{\partial x} + \frac{\partial w_p}{\partial z}\right) = -\rho_p g + \rho_p\frac{\partial^2 w_p}{\partial t^2} \tag{36}$$

where G_p=shear modulus of the pipeline; μ_p=Poisson's ratio of the pipeline; ρ_p=pipe's density; u_p and w_p=displacement components of the pipeline.

3. Model verification

In this section, the constitutive model parameters will be calibrated, based on the specified soil properties, and then the authors will validate the developed framework against the wave flume test (Sumer et al., 2006) and geotechnical centrifugal test (Miyamoto et al., 2020). In this way, the developed model can reliably predict the vulnerability to liquefaction of seabed around an embedded pipeline.

3.1. Comparison with the wave flume test

Sumer et al. (2006) experimentally investigated the pore-water pressure response around a pipeline embedded in a silty seabed through a series of wave flume tests. The numerical setup is similar to the soil box allocated to the wave flume which is 0.17 m deep and 0.9 m long (equivalent to the wavelength), while the pipeline is embedded at a certain depth along the centreline of the computational domain. The same parameters suggested by Sumer et al. (2006) were used here: water depth (d)=42 cm; wave period (T)=1.6 s; wave height (H)=16.6 cm; pipe burial depth (e)=10.5 cm; pipe diameter (D)=8 cm; soil permeability (k)=5×10^{-8} m/s; void ratio (e)=0.54; degree of saturation (S_r)=100%. While the selection of material parameters seems to be cumbersome, M_{f0}, M_{g0}, G_0 and K_{ev0} can be directly determined based on the properties of silty sand given by Sumer et al. (2006). Table 1 shows the constitutive parameters considered in this test.

Table 1: Model parameters

Parameter	Silty sand	Silica sand No. 7	Unit
K_{ev0}	1500	1982.4	kPa
G_0	1620	2100	kPa
M_{g0}	1.46	0.7	–
M_{f0}	1.2	0.46	–
α_0	0.45	0.01	–
β_0	4.2	0.2	–
β_1	0.2	2.5	–
H_0	750	700	kPa
H_{U0}	40,000	1,000	kPa
γ_U	6.0	6.0	–
a	0.1	0.3	–
b	0.1	0.5	–

Figure 1 shows the measured and simulated results at the bottom and in the far field at the same level as the pipeline with regards to the evolution of pore water pressure. To demonstrate the advantage of this developed model, the results without considering the impact of PSR are included as a reference. It is found that the predicted results agree fairly well to the experimental data at the bottom of the pipe and in the far field. This is evidenced by the perfect match on the magnitude of pore water pressure as well as the number of cycles to cause liquefaction at which the pore water pressure stabilised. However, while the model ignoring the impact PSR can qualitatively agree with the experimental findings, the increased rate of pore water pressure was significantly underestimated.

*3.2. Comparison with the geotechnical centrifugal test*

Miyamoto et al. (2020) carried out a series of regular and irregular wave experiments on the vulnerability to liquefaction of an embedded pipeline in a drum centrifuge under an acceleration of 70 g. To reproduce centrifugal wave tests, the numerical model was established on a prototype scale with a scaling factor of 70, and used the following parameters: water depth
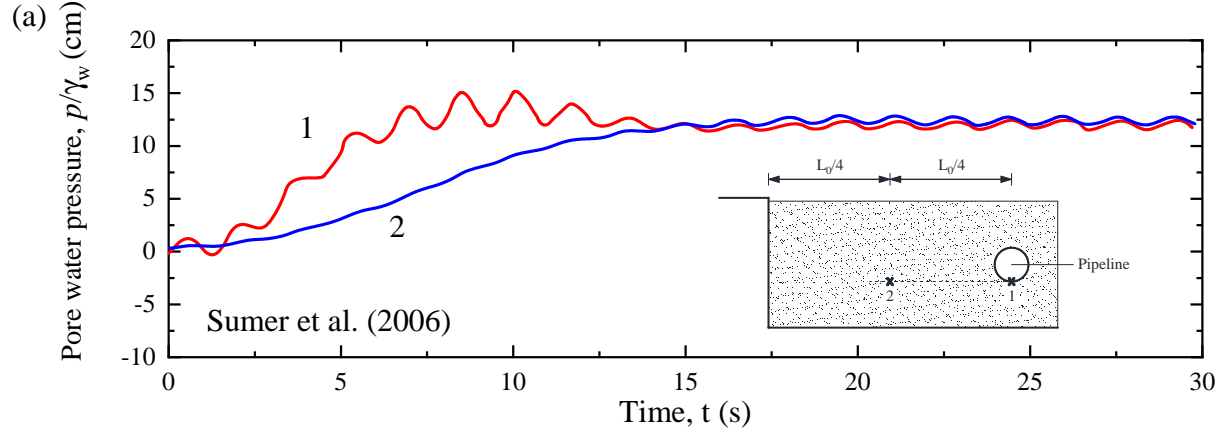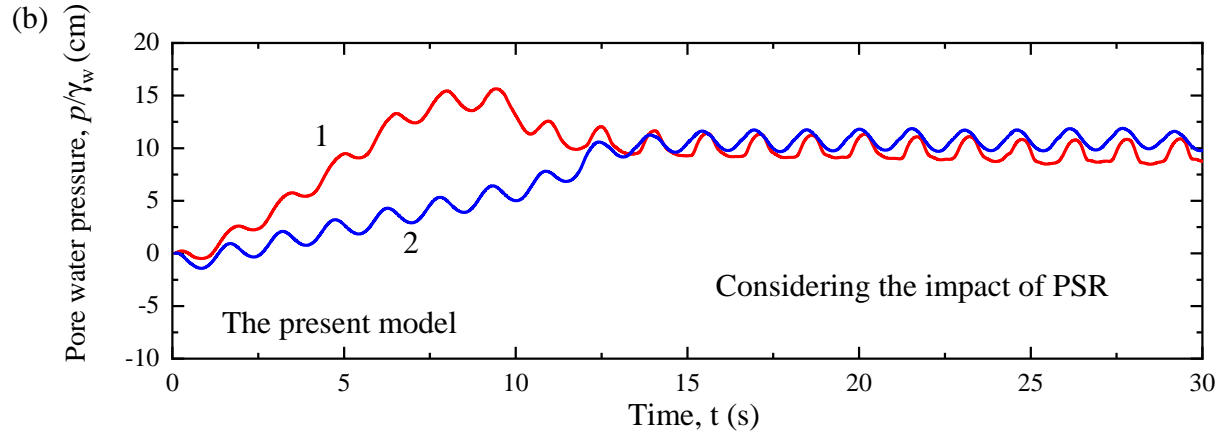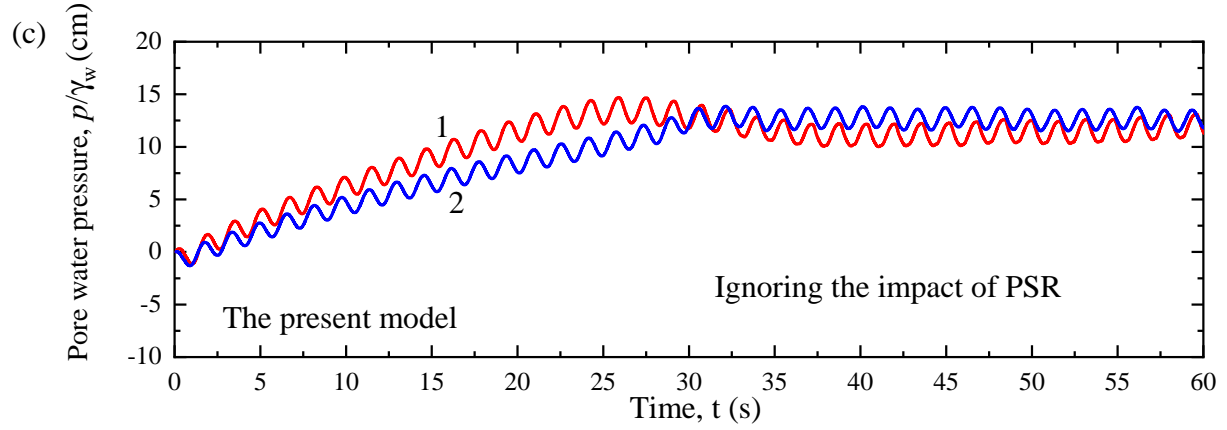
Figure 1: Time histories of the pore water pressure at the pipe bottom and in the far field for (a) measured results Sumer et al. (2006), (b) predicted results with and (c) without considering the impact of PSR.

(d)=7 m; period of significant wave ($T_{1/3}$)=7 s; significant wave height ($H_{1/3}$)=2 m; pipe diameter (D)=1.75 m; pipe burial depth (e)=2.765 m; seabed thickness (h)=7.14 m; soil permeability (k)=1.5×10^{-4} m/s; void ratio (e)=1; degree of saturation (S_r)=100%. The constitutive parameters were selected for the loosely formed sandy bed (Silica sand No. 7) considered in the test, as given in Table 1.

Figure 2 shows the time histories of irregular wave-induced pore water pressure at three different depths and 53 mm from the centreline of the pipeline, together with the hydrodynamic pressure at the soil surface (i.e., top panel of Fig. 2). It was found that the predicted results attained an acceptable match with the laboratory data. In particular, the number of cycles predicted for the onset of liquefaction was essentially the same as in the centrifugal test at all depths of soil. This indicates that the developed model can reliably predict the pore water pressure in a liquefiable seabed due to storm wave loading.

4. Model applications

4.1. Problem considered

Figure 3 illustrates how the present model is applied to investigate on a prototype scale, the pipeline and seabed as they are affected by realistic storm waves. In this study, the authors considered that a pipeline with an outside diameter (D) and burial depth (e) was fully embedded in a 300×20 m silty seabed, while presuming irregular storm waves at the still water level ($z = d + h$) at a water depth (d) was travelling along the x-direction. Table 2 provides all parameters considered in the following numerical simulations. It is noteworthy that different values of pipe specific gravity have been considered in this study as pipe material, wall thickness and density of fluid that pipe carry may vary considerably to different installation or operating conditions in the candidate site. Sumer et al. (1999) carried out wave flume tests to investigate the sinking/flotation of a fully buried pipeline in the course of liquefaction in which a wide range of pipe specific gravity was considered (i.e. $1 \leq \gamma_p/\gamma_w \leq 8.9$). In this study, the pipeline having a specific gravity equivalent to the total specific weight of the soil, i.e., $\gamma_p = \gamma_t \approx 2\gamma_w$, was taken as a typical case involved in majority of the analysis unless other values were indicated in the parametric study.

To specify the mechanisms of wave-seabed-pipeline interactions during an ocean storm, the following boundary conditions are employed in the geotechnical model:
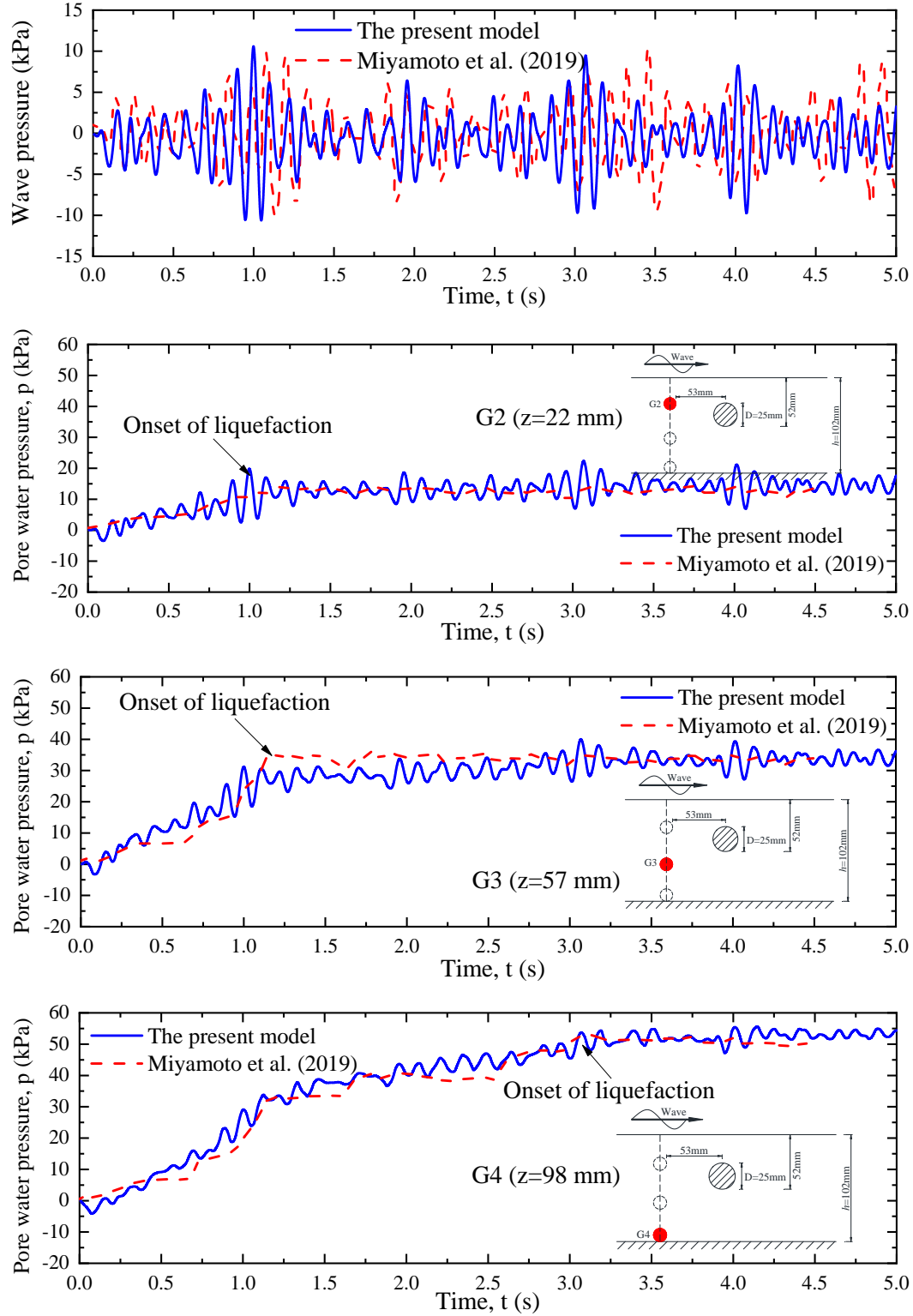
Figure 2: Predicted and measured results of pore water pressure at the pipe vicinity under irregular wave loading.
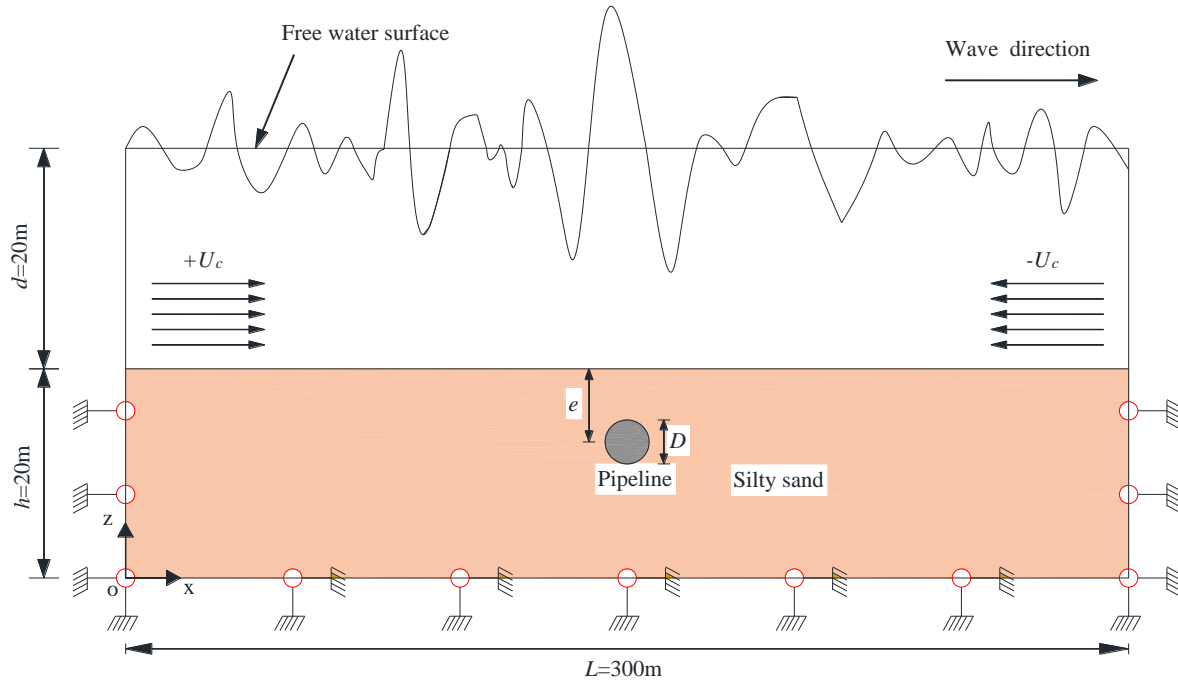
Figure 3: Schematic illustration of the scenario considered in this study (Not in scale)

Table 2: Input data in the numerical examples.

Description	Characteristics	Value	Unit
Characteristics of ocean storms			
Significant wave height	$H_{1/3}$	4 or various	[m]
Water depth	d	20	[m]
Period of significant wave	T_p	11.8	[s]
Current velocity	U_0	1.5	[m/s]
Soil characteristics			
Permeability	k_s	1.0×10^{-6} or various	[m/s]
Porosity	n_s	0.35	–
Initial void ratio	e_0	0.54	–
Degree of saturation	S_r	100	%
Pipeline characteristics			
Young's modulus	E_p	3×10^7	[kPa]
Poisson's ratio	μ_p	0.2	–
Pipe diameter	D	1.5	[m]
Pipe burial depth	e	2 or various	[m]
Pipe specific gravity	γ_p	20 or various	[kN/m^3]

1. The base of the computational domain is rigid and impermeable:

$$u = w = 0 \ \text{ and } \ \frac{\partial p}{\partial z} = 0 \ \text{ at } \ z = 0 \tag{37}$$

2. Both sides are fixed in the direction normal to the boundary. Since the pipeline was embedded with long distances from the lateral sides the adverse effect of fixed boundaries can be omitted.

$$u = 0 \ \text{ and } \ \frac{\partial p}{\partial x} = 0 \tag{38}$$

3. The pipeline is assumed to be impermeable and have zero flow flux normal to its outside surface, i.e.

$$\partial p / \partial n = 0, \ \text{ at } \ r = \sqrt{(x - x_0)^2 + (z - z_0)^2} = D/2 \tag{39}$$

4. Pore water can freely drain out from the seabed where the shear stress and vertical effective normal stress vanish, whereas the pore water pressure is consistent with the hydrodynamic pressure at the surface of the numerical wave flume (P_b).

$$\sigma'_z = \tau_{zx} = 0 \ \text{ at } \ z = 20m, \ \ p(x, h; t) = P_b(x; t) \tag{40}$$

A numerical wave flume is established by specifying a pressure outlet at the atmospheric boundary while a slip boundary condition is considered at the bottom. In the hydrodynamic simulation, a real storm recorded by Franco et al. (1999) was reproduced based on the JONSWAP spectrum with M=100. A recording length of about 20 min was considered and a data sampling interval of 1/10–1/20 of the significant wave period is recommended. To generate and/or absorb storm waves superimposed onto a stable ocean current, the IHFOAM (also named as OlaFlow) toolbox (Higuera et al., 2013) was utilised by applying the Static Boundary Method (SBM). More details regarding the generation/absorption of water waves within the context of OlaFlow can be found by referring to work by Higuera and his co-workers (Higuera et al., 2013, 2014a,b).

4.2. Effect of principal stress rotation (PSR)

Figure 4 shows the prediction of the present model in time series of the pore water pressure and vertical effective stress at two locations, and for various wave heights with or without considering the impact of PSR. Note that Figures 4(a1) and (b1) depict the results at the pipe bottom while Figures 4(a2) and (b2) are their counterparts showing how liquefaction develops in the undisturbed-flow situation without the presence of the pipeline. In each case with successive irregular wave loads, there was a one-to-one correspondence between the pore water pressure and vertical effective stress in the time history curves. Apparently, the rate of increase in pore water pressure and associated decrease in the vertical stress accelerated significantly, when the impact of PSR was considered; this caused the soil beneath the pipe and in the far field to quickly liquify at a low number of loading cycles (t/T_p=11 and 15, respectively), whereas more wave cycles were need to cause liquefaction in the non-PSR case, even with larger waves. Regardless of whether PSR was included or not, the pore water pressure at the bottom of the pipeline always developed faster than that in the far field at the same level. While this was consistent with the wave flume test (Teh et al., 2003; Sumer et al., 2006), on a prototype scale analysis, it may be further affected by the pipe specific gravity, an issue that will be discussed in later sections.

Figure 5 shows the distribution of relative difference in period-averaged pore water pressure between cases where the impact of PSR along two selected sections and at five loading phases have been and have not been considered. Here, all relative differences were normalised by the amplitude of hydrodynamic pressure exerted onto the seabed surface (P_0), which is determined based on the linear wave theory. At the incipient loading stage (i.e. $t/T_p \leq 10$), where the degrees of stress axis rotations remained marginal, the relative difference was not that significant, particularly in deeper locations; however, it did become more pronounced in the subsequent loading phases and increased with successive wave loads. The effect that PSR had on the residual pore water pressure became more significant closer to the pipe, where the maximum discrepancy along the centreline of the pipe can reach up to 85% after t/T_p=25, compared to 80% in the far field region.

The above analysis indicate that the rate of accumulated pore water pressure is more pronounced at the pipe bottom compared to that in the undisturbed-flow situation particularly when
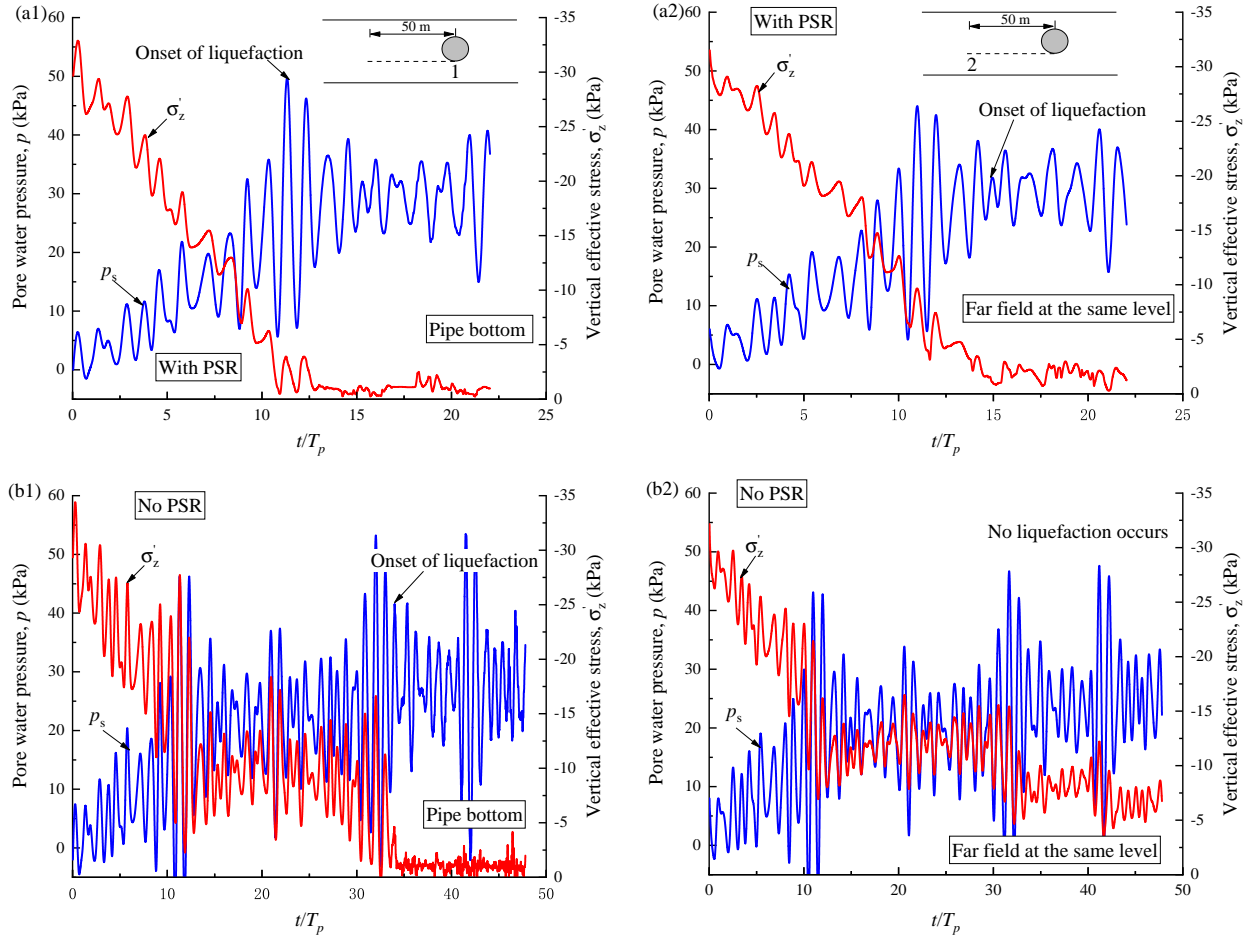
16

Figure 4: Time histories of pore water pressure at the pipe vicinity and in the far field (a) with or (b) without considering the impact of PSR.
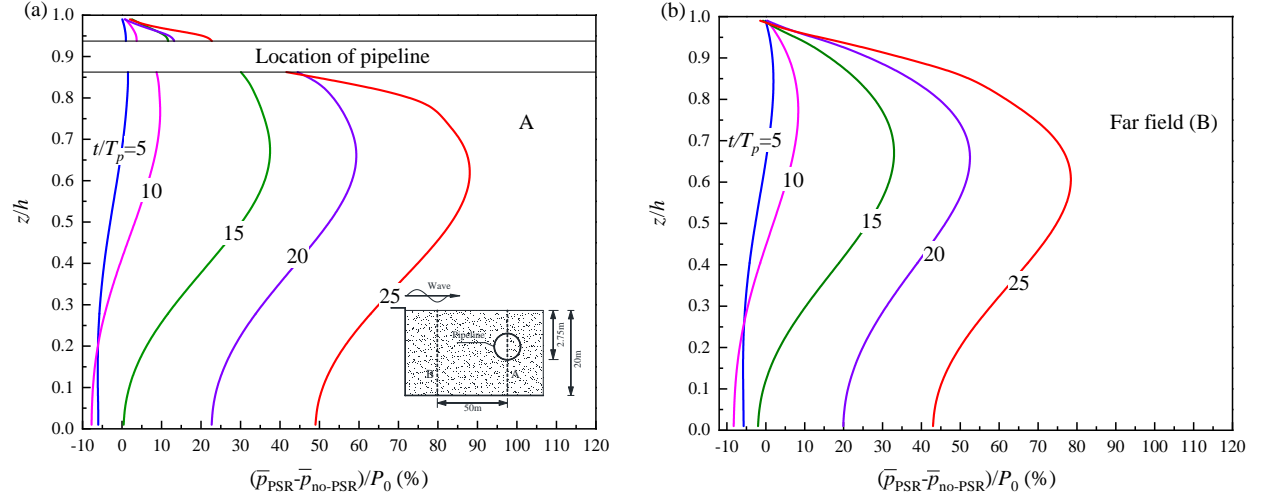
Figure 5: Distribution of residual pore water pressure at different loading phases along (a) centerline of the pipeline, and (b) the cross section in the far field.

the impact of PSR is considered. For shallowly embedded pipeline where there is an engagement between water flow field and the soil seepage field below the pipeline such kind of pressure differences may lead to an additional seepage flow below the pipeline and cause the onset of tunnel erosion (Sumer and Fredsøe, 1990; Chiew, 1990; Kazeminezhad et al., 2012; Shi and Gao, 2018). For the scenario considered in this study where the pipeline is fully embedded into the seabed local scour or tunnel erosion may not be of great concerns (Fredsøe, 2016).

4.3. Difference of seabed response between regular and irregular wave loading

Figure 6 shows the variations in depth of residual pore water pressures at five loading phases along the centreline of the pipe and in the far field. The predicted results under a regular wave loading with wave heights and periods (i.e., $H_r = H_{1/3}/\sqrt{2}$ and $T_r = \overline{T}$) that are equivalent to irregular wave conditions were used as benchmarks for comparison. Here, $\overline{T}$ denotes the mean zero upcrossing period of the generated storm waves. Note that the dashed line in Figure 6 represents the initial vertical effective stress that identifies the onset of liquefaction when $\bar{p} = -\sigma'_{z0}$. During ocean storms the potential for liquefaction close to the pipe or further away are progressive in nature because liquefaction advances downwards as the residual pore water pressure increases with successive wave loads. Moreover, the presence of a pipeline accelerates the downward advance of liquefaction directly below the pipeline to depths of up to 0.3h at
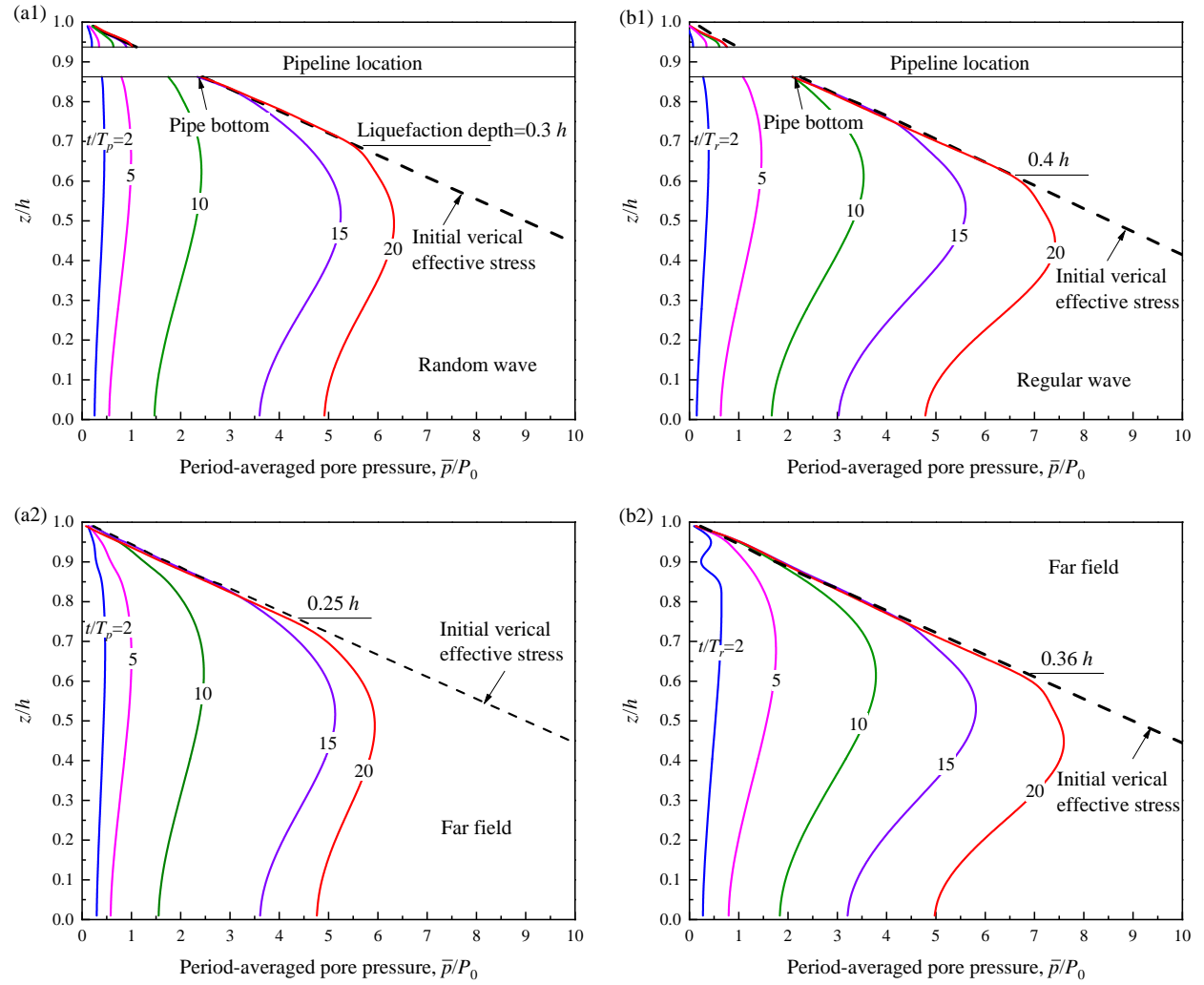
18

Figure 6: Variations in depth of normalised residual pore water pressure at different loading phases close to the pipe and in the far field under (a) irregular wave loading, and (b) regular wave loading.
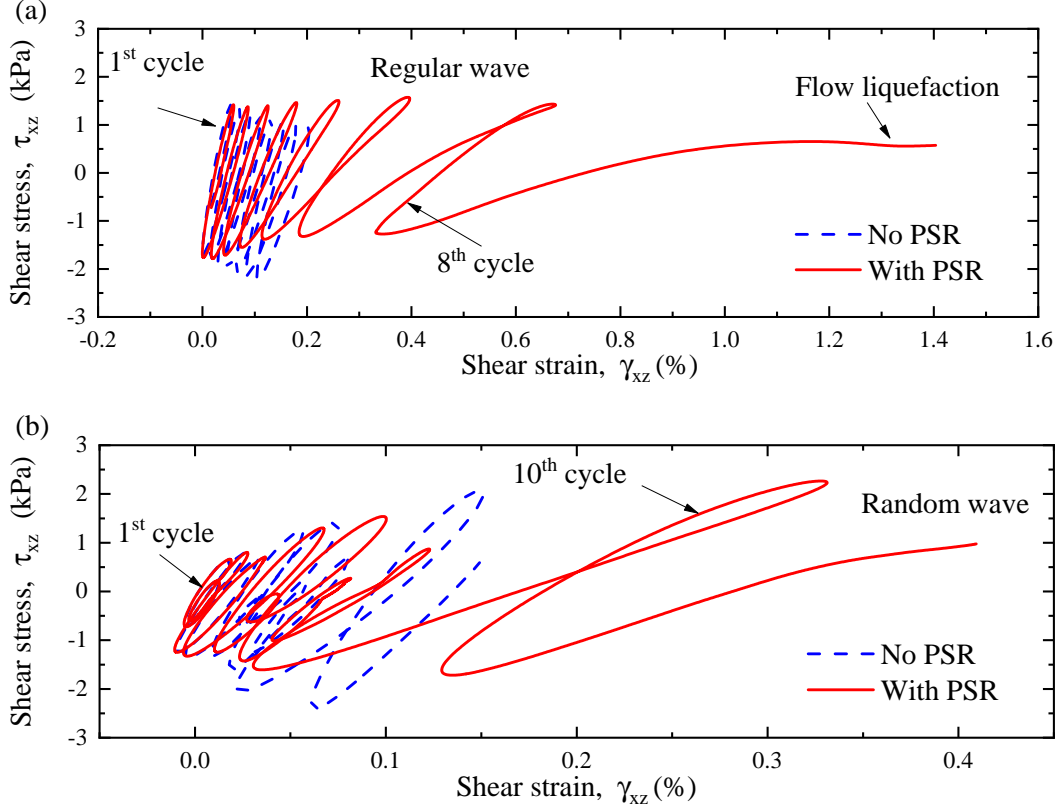
Figure 7: Predicted shear stress versus shear strains at the pipe bottom under (a) representative regular wave loading, and (b) irregular wave loading.

t/T_p=20, whereas liquefaction is only 0.25h deep further away. Similarly, the progress of liquefaction under regular waves is faster than under irregular waves, although in the latter case there was a sharp increase in the depth of liquefied soil during the time range [10T_p, 15T_p], where the seabed soil may experience the most severe waves at a resonant loading condition. From a practical perspective, irregular waves should be simulated when designing ocean pipelines, because the sudden rise in pore water pressure may lead to a significant degradation of foundation soil exposed to ocean storms, even though simulating regular waves may be more conservative.

Figure 7 shows the evolution of shear stress versus shear strains induced in soil at the pipe bottom due to different types of wave loads. It is predicted that liquefaction takes place very quickly within approximately 8 cycles of regular waves; this is manifested by an almost vanished shear stress (i.e., no stress reversal) and extensive shear strain in tandem. Under irregular wave conditions the failure pattern differs with regards to the extent of plastic deformation; Figure 7(b) shows that even after 10 wave cycles there was sufficient stress reversal, but no flow

20

liquefaction because, as Figure 7(b) shows, the number of waves that affected the evolution of pore pressure and subsequent softening of soil was less than regular waves. However, where the impact of PSR was ignored, the predicted hysteresis loops were confined to a small shear strain (lesser than 0.2 %) after 10 wave cycles because in both cases there was no significant degradation of shear stiffness.

4.4. Effect of pipeline weight

As the authors mentioned earlier, on a prototype scale analysis, the pipe specific gravity may affect the vulnerability of soil to liquefaction in the neighbouring region (Zhao et al., 2014, 2018b). This issue will be further addressed in this section by incorporating various specific gravities in the consolidation analysis and in the subsequent dynamic analysis of wave, seabed, and pipeline interactions.

Figure 8 shows the evolution of period-averaged pore water pressure at four loading phases around the pipe perimeter for three different specific gravities, together with the initial vertical effective stress obtained at the end of the consolidation phase, based on the pre-consolidation analysis. Note that the case with an almost equivalent specific pipe gravity to the total specific weight of the soil (i.e., $\gamma_p = \gamma_t \approx 2\gamma_w$) was used as a benchmark for comparison. As shown in Figure 8(a), the process of liquefaction close to the pipe was similar to the wave flume tests (Teh et al., 2003; Sumer et al., 2006), that is, liquefaction begins at the bottom of the pipe and then spreads upwards around the perimeter. As the pipe specific gravity increases, as shown in Figure 8(b)&(c), there is a distinct difference with regards to the distribution of initial vertical effective stress as well as rate of increased pore pressure around the pipe. Unlike those shown in Figure 8(a), the predicted liquefaction in Figure 8(b) and (c) with larger γ_p/γ_w began at the top of the pipe and then spread downwards around the perimeter. A relationship between the number of cycles to cause liquefaction (N_L) and the various levels of pipe specific gravity γ_p/γ_w is shown in Figure 9. Here the top of the pipe N_L decreased as γ_p/γ_w increased, which is opposite to the bottom of the pipe. There is a critical point of intersection on the curves (i.e., γ_p/γ_w=2.48) beyond which the soil at the pipe bottom had a higher cyclic resistance to liquefaction. Interestingly, Figure 8 shows that in every case, liquefaction occurred with less cycles in the upstream region than that in the downstream region of the pipe. This was probably due to differences in the stagnation pressure between these two regions as a result of the asymmetric profile of storm waves considered in this study.
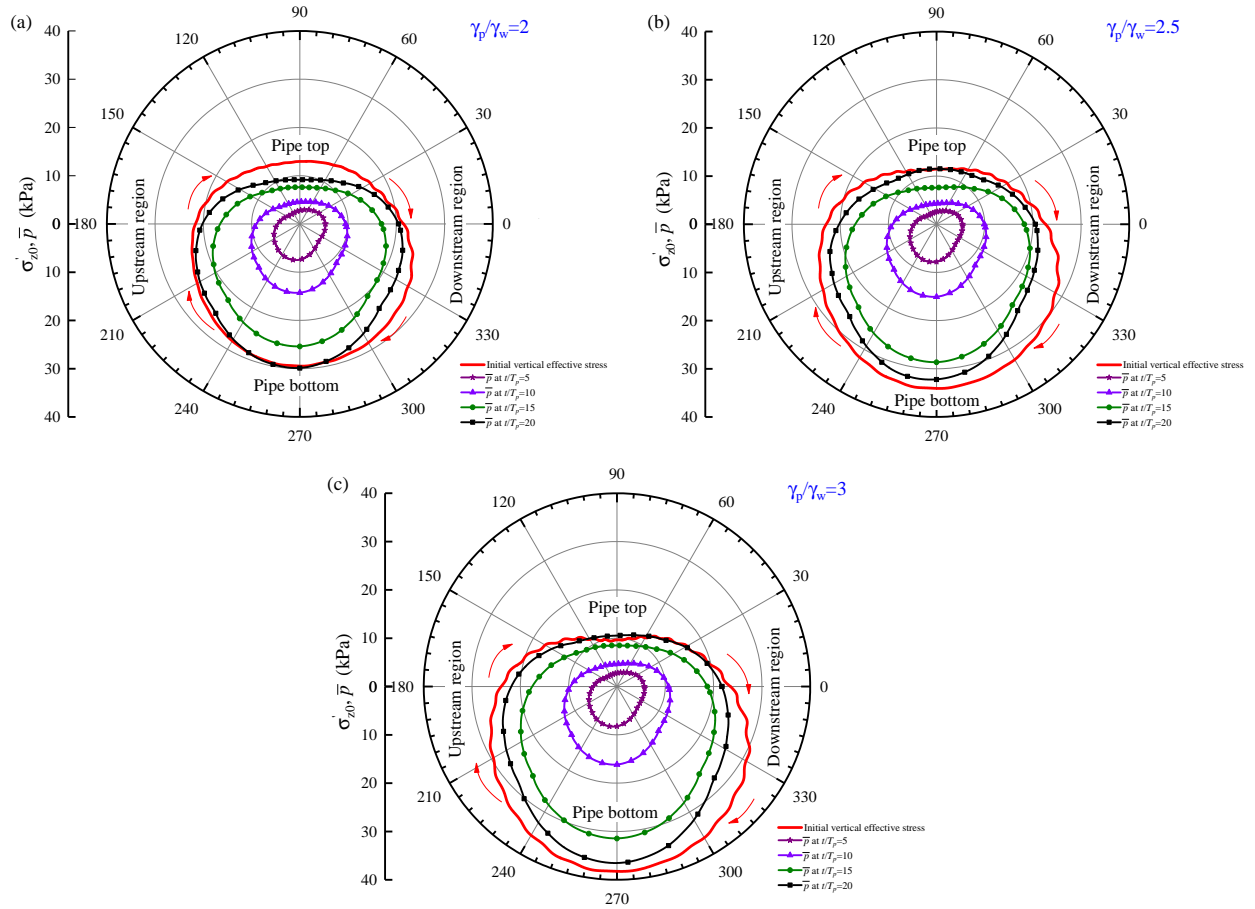
21

Figure 8: Evolution of residual pore water pressure around the pipe perimeter for various pipe specific gravities.

4.5. Effect of current

Figure 10 shows snapshots of the pore pressure for three different cases of irregular waves, and waves with following and opposing currents at two selected loading phases. Here the authors consider the severest condition that a real scenario may encounter during ocean storms where a current velocity may reach up to 1.5 m/s associated with the ocean storm wave motions (Cieślikiewicz et al., 2017). The predicted results indicate that under irregular waves, the pore water pressure was not distributed uniformly between successive cyclic loads, as was the case for regular waves. Under co-current waves (i.e., waves that propagate in the same direction as the current), the pore water pressure developed faster due to the longer wave length and intensified loading magnitude, unlike the case without a current. Whereas the counter-current wave (i.e., waves that coexist with an opposing current) does the opposite. The enlarged results (Figures 10(a1)&(b1)) shows how the evolution of pore water pressure was disturbed by the
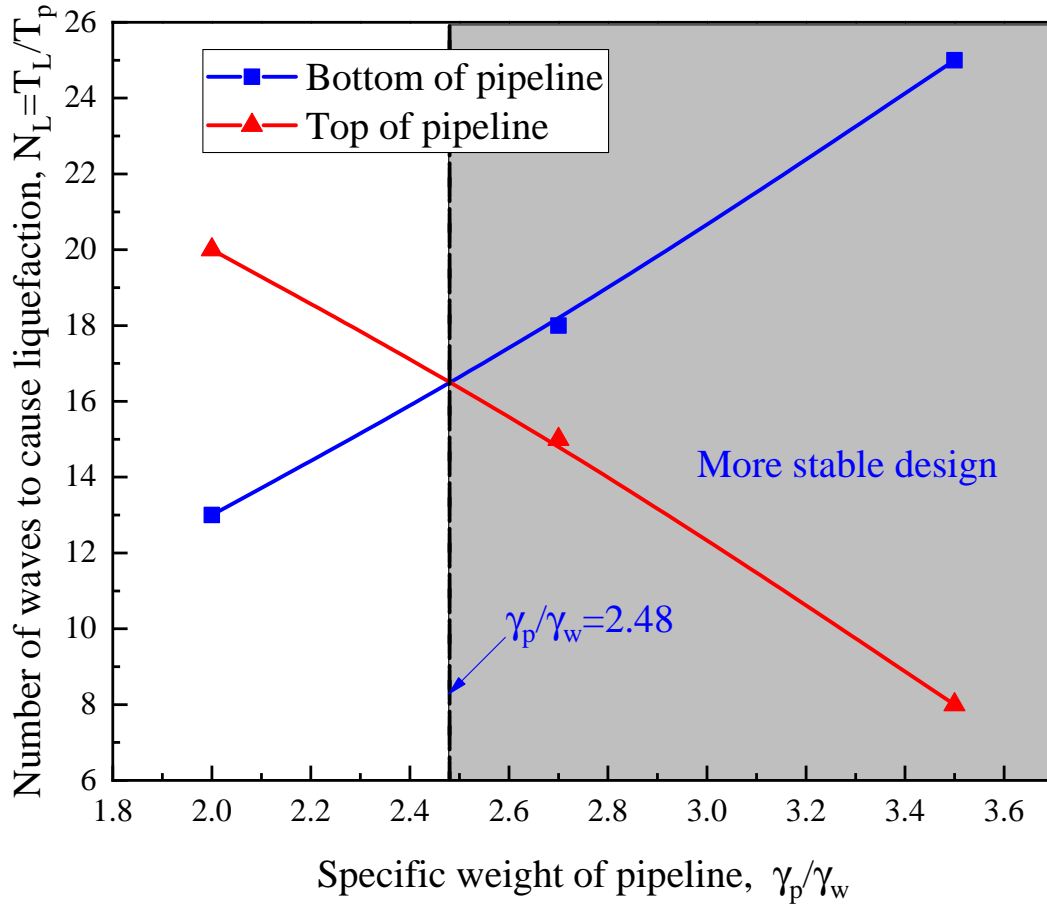
22

Figure 9: A relationship between pipe specific gravity and the number of waves needed to cause liquefaction at the top/bottom of the pipeline.

presence of a pipeline in its neighbouring region. As shown in Figure 10, the accumulated pore pressure was higher at the upstream region of the pipe, but with successive wave loads the pore water pressure was distributed more uniformly in the direction of wave propagation, as was the residual liquefaction due to progressive waves (Zhao et al., 2014).

Figure 11 shows the variations in soil depth of the relative differences between waves with and without a current, with regards to the residual pore water pressure at four selected loading phases. It was expected that the residual pore water pressure predicted for co-current waves would be greater than for waves alone, whereas with the counter-current case, the predicted residual pore water pressure was slightly smaller than the wave alone case. In general, the magnitude of relative difference increased with successive wave loads, but this increased rate in the lower part of seabed was higher than in the upper seabed where the pore water pressure had already stabilised due to the onset of liquefaction. Moreover, a following current had a
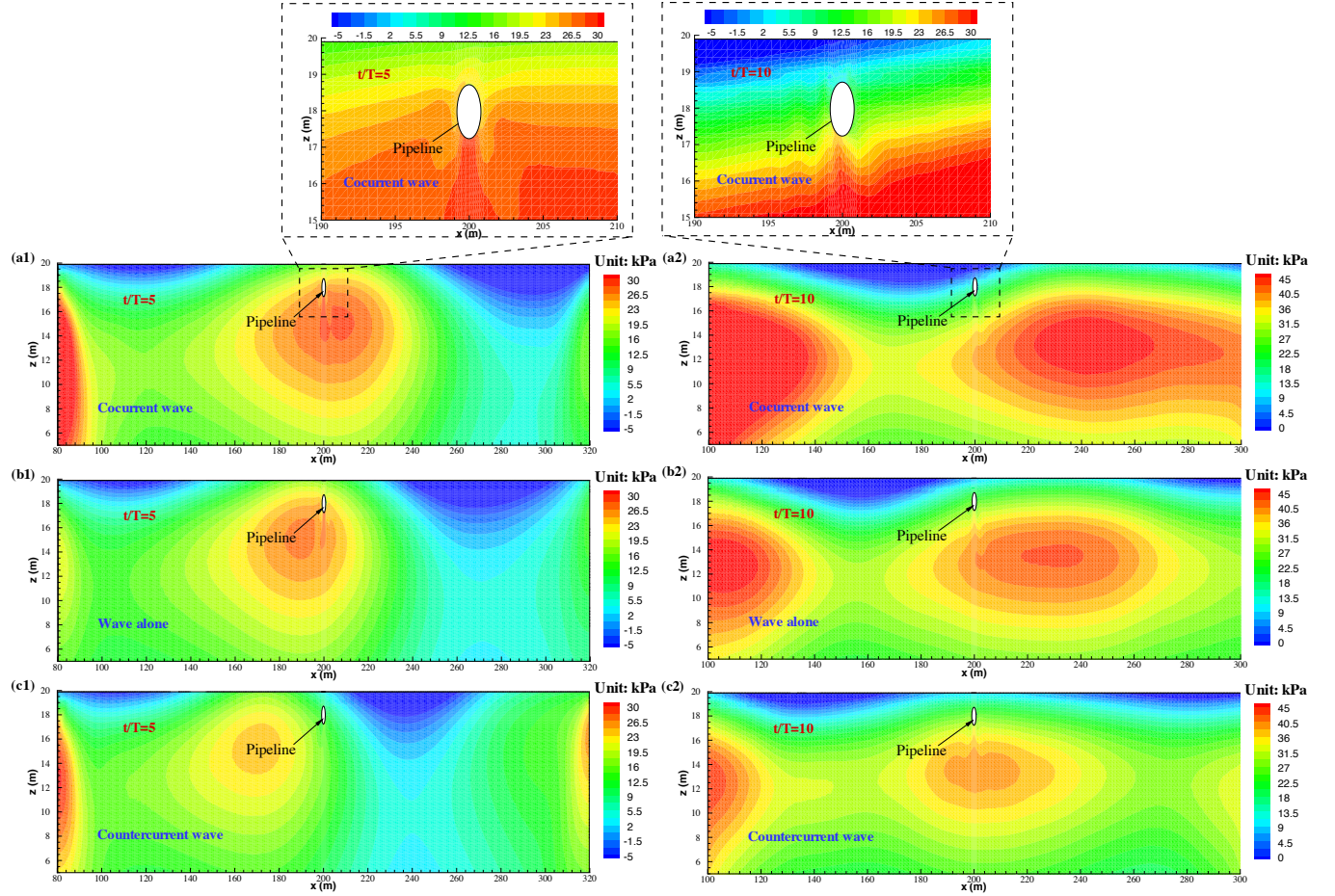
Figure 10: Snapshots of predicted pore water pressure at two loading phases for (a) waves that coexist with a following current, (b) waves only, and (c) waves that coexist with an opposing current.
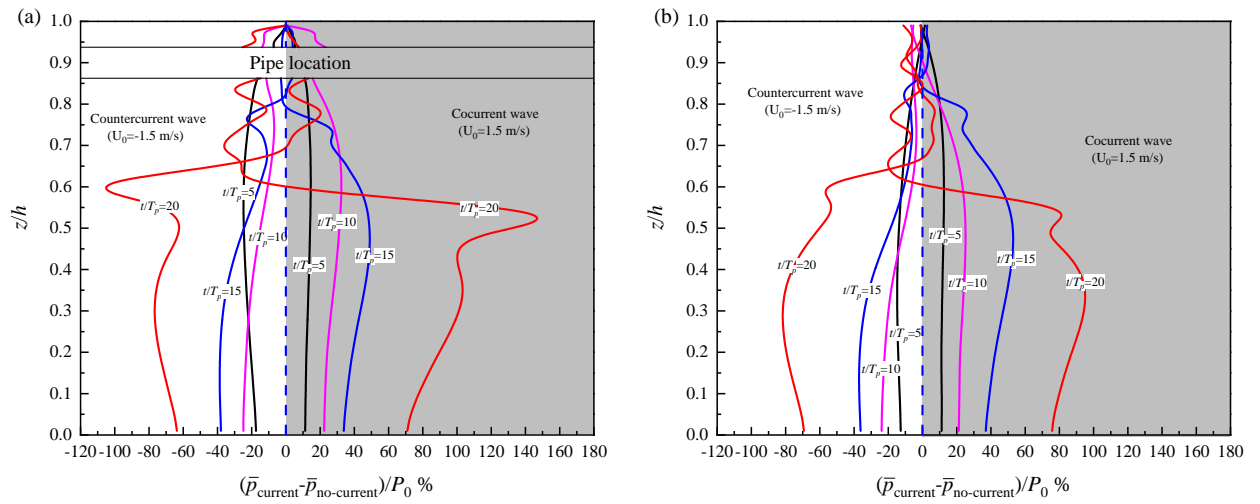

Figure 11: Effects of a current on the residual pore water pressure induced by storm waves (a) close to the pipe, and (b) in the far field.
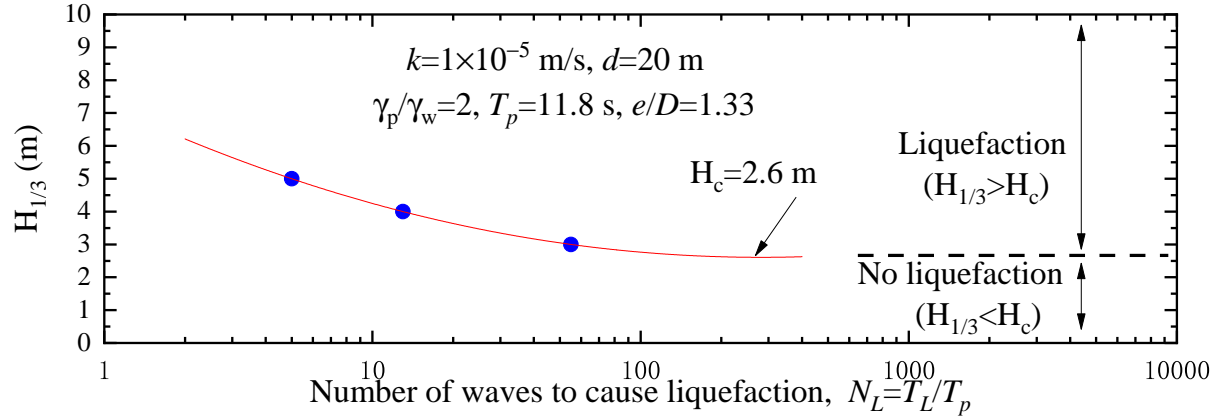
Figure 12: The number of waves needed to cause liquefaction at the pipe bottom as a function of wave height.

more apparent effect on the evolution of residual pore water pressure, particularly close to the pipe. For example, after 20 successive wave loads the maximum relative difference could be up to 150% in co-current waves close to the pipe and 100% in the far field, while the maximum relative difference between the counter-current waves were 105% and 80% close to the pipe and in the far field, respectively. This means that ignoring the current may lead to inappropriate design, especially close to the pipeline.

4.6. Design of pipeline exposed to ocean storm

In engineering practice, a trench layer composed of coarse gravel (artificial backfill) or fine sand (natural backfill) with a wide range of permeability has been normally used to counter the inherent instability of a pipeline on a liquifiable seabed. For design purposes, this section will provide an empirical method by which engineers can select feasible backfilling materials to mitigate the liquefaction hazard at the operational stage when pipelines are exposed to ocean storms.

Figure 12 shows the number of waves required to initiate liquefaction at the pipe bottom as a function of wave height. Obviously, the smaller the waves, the less cyclic shear stress will be generated in the seabed soil, and the longer duration of ocean storms is needed to cause liquefaction. As with the experimental findings of de Alba et al. (1976) and Sumer et al. (1999), as the number of irregular waves increases, the wave height that affects the shear stress to cause liquefaction tends to be an asymptotic value below which liquefaction no longer occurs. Remember that the pipe specific gravity may vary according to operational requirements. Figure
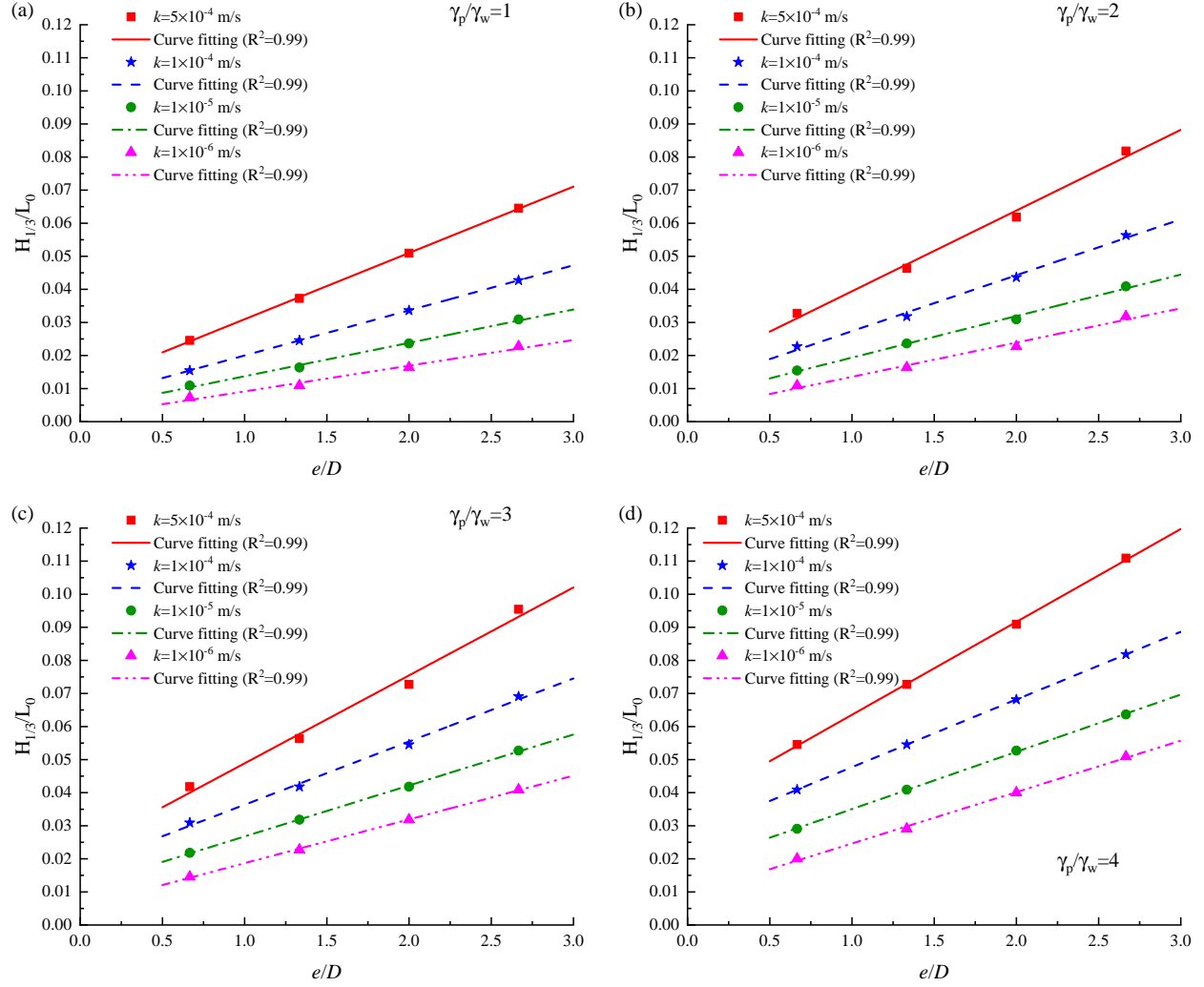
25

Figure 13: The relationship between normalised critical wave height and normalised pipe burial depth

13 shows how the normalised specific gravity of pipe (γ_p/γ_w), the normalised burial depth (e/D), and the drainage condition of backfilling material (k), will affect the normalised critical value of wave heights (H_c/L_0) that are large enough to trigger liquefaction. It is predicted that for each value of γ_p/γ_w or k there is an almost linear relationship between H_c/L_0 and e/D with a regression coefficient that is higher than 0.99. On this basis, an empirical formulation is proposed herein

$$\frac{H_c}{L_0} = a_d \left(\frac{e}{D}\right) + b_d \tag{41}$$

The coefficients a_d and b_d in (41) for various operational pipe specific gravities and drainage conditions of a trench layer are plotted in Figure 14. With this design chart and the empirical
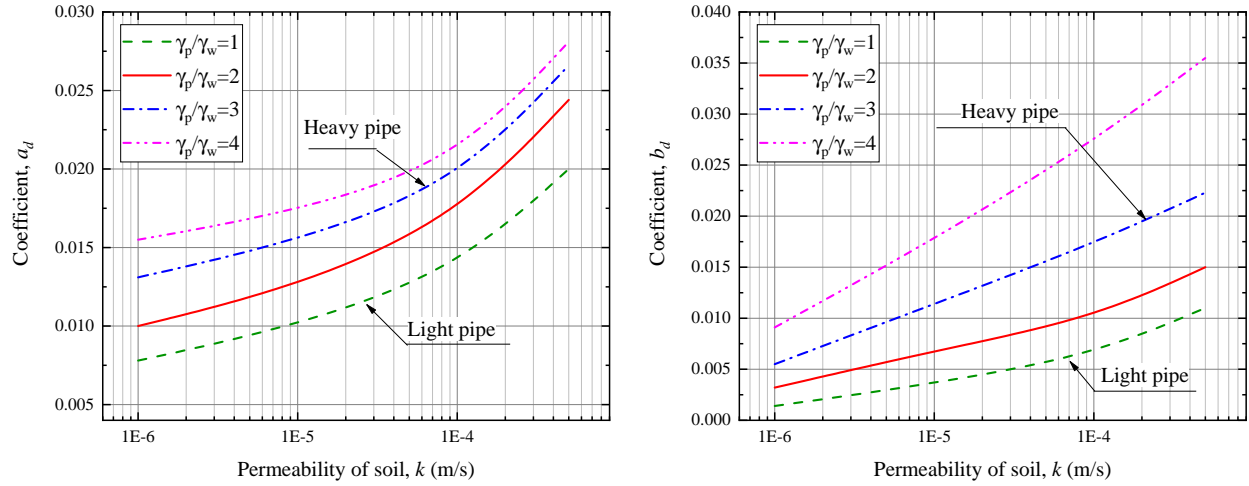
26

Figure 14: Design graphs for determining the coefficients in the empirical formulation.

formulation, (41), pipe engineers are able to design a trench layer by controlling the drainage condition of the backfilling material with the following procedures:

1. For specific operational pipe gravity, select feasible backfilling material and then determine the two coefficients (a_d and b_d) from the design chart (Figure 14).

2. With these coefficients, the relationship between H_c/L_0 and e/D can be determined from (41).

3. By substituting the designed value of burial depth e/D, the critical wave steepness (H_c/L_0) needed to cause liquefaction can be determined.

4. Compare the calculated H_c/L_0 against the storm wave conditions on the candidate site to verify that the selected backfill material is capable of protecting the pipeline based on site conditions and operational requirements.

Fig.15 shows the relationship between empirical and numerical predictions of the critical wave height (H_c) for nine different cases with a combined variations of e/D, γ_p/γ_w, L_0 and k. It can be seen that the points of H_c predicted by Eq. 41 and that predicted by the developed model are basically in a straight line at an inclination of 1. This indicates that the proposed empirical equation is applicable to various site and operational conditions in predicting the critical wave steepness to meet the design requirement.
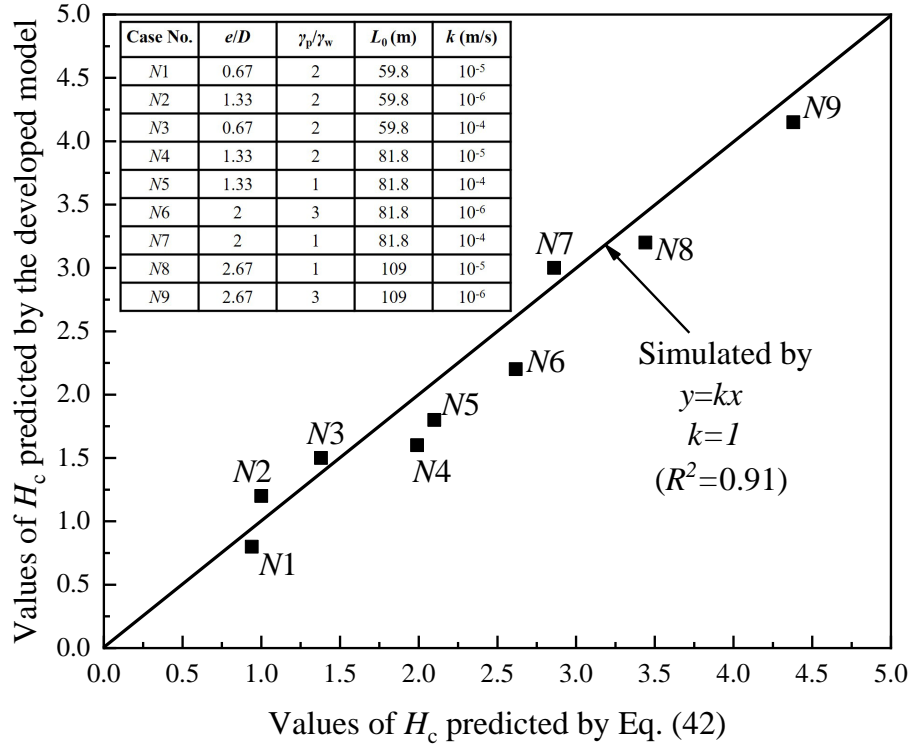
Figure 15: H_c predicted by Eq. (42) versus H_c predicted by the developed model.

5. Conclusions

In this paper, an integrated numerical model was developed to investigate the vulnerability to liquefaction of an embedded pipeline under the influence of irregular waves and current loading that match real ocean storms. The influence of pipe specific gravity, the irregularity of storm waves, and the presence of currents on the residual pore water pressure close to the pipe and/or further away, was compared and evaluated using quantitative analysis. An empirical method to design a trench layer as a countermeasure against liquefaction has also been proposed. Based on the analysis presented in this paper, the following salient conclusions can be drawn.

1. In the context of the integrated framework developed, the use of a modified PZIII model with PSR-induced deformation in the constitutive relationship of the soil shows a more promising comparison with the wave flume test. Ignoring the impact of PSR may lead to a significant underestimation of the rate in the accumulated pore water pressure and the potential for liquefaction during ocean storms, particularly close to the pipe rather than further away.

2. Silty sand close to and further away from the pipe is more susceptible to liquefaction due to regular rather than irregular waves. This is because in the latter case there are less number of waves that could effectively facilitate the build-up of pore water pressure, although there are resonant loading conditions which could lead to a sharp increase in the residual pore water pressure.

3. The presence of a pipeline may simultaneously affect the evolution of pore water pressure and the distribution of initial stress field (at the end of consolidation phase) in its neighbouring region. In the case of $\gamma_p/\gamma_w \leq 2.48$, liquefaction commenced at the pipe bottom, and then spreads upward around the perimeter; this was consistent with the wave flume test. Conversely, for heavier pipe (i.e., $\gamma_p/\gamma_w \geq 2.48$), the onset and spread of liquefaction showed an opposite trend.

4. The effect of a following current was more apparent than an opposing current on storm wave-induced liquefaction close to the pipe and further away. After 20 successive storm wave loads, ignoring the presence of a current may lead to an underestimation and an overestimation of the relative difference (i.e. $(\bar{p}_{current} - \bar{p}_{no-current})/P_0$) by 150% and 105% in the co-current waves and counter-current waves.

5. There is a critical wave height below which the number of waves required to cause liquefaction approaches infinity. A distinct relationship between the critical wave height, pipe burial depth, pipe specific gravity and drainage condition of the backfilling materials was proposed so that pipe engineers can design a trench layer with backfilling materials that will mitigate liquefaction.

6. Acknowledgements

References

Cai, Y. Q., Sun, Q., Guo, L., Juang, C. H., Wang, J., 2015. Permanent deformation characteristics of saturated sand under cyclic loading. Canadian Geotechnical Journal 52 (6), 795–807.

Chan, A. H. C., 1995. User mannual for diana-swandyne ii-dynamic interaction and nonlinear analysis swansea dynamic program version ii. Tech. rep., School of Civil Engineering, University of Birmingham, UK.

Chiew, Y. M., 1990. Mechanics of local scour around submarine pipelines. Journal of Hydraulic Engineering 116 (4), 515–529.

Christian, J. T., Taylor, P. K., Yen, J. K. C., Erali, D. R., 1974. Large diameter underwater pipeline for nuclear power plant designed against soil liquefaction. In: Proceeding of Offshore Technology Conference. pp. 597–606.

Cieślikiewicz, W., Dudkowska, A., Grusza, G., Jedrasik, J., 2017. Extreme bottom velocities induced by wind wave and currents in the gulf of gdańsk. Ocean Dynamics 67, 1461–1480.

Damgaard, J. S., Sumer, B. M., Teh, T. C., Palmer, A. C., Foray, P., Osorio, D., 2006. Guidelines for pipeline on-bottom stability on liquefied noncohesive seabeds. Journal of Waterway, Port, Coastal and Ocean Engineering, ASCE 132 (4), 300–309.

de Alba, P., Seed, H. B., Chan, C. K., 1976. Sand liquefaction in large-scale simple shear tests. Journal of Geotechnical Division, ASCE 102, 909–928.

Dunn, S. L., Vun, P. L., Chan, A. H. C., Damgaard, J. S., 2006. Numerical modeling of wave-induced liquefaction around pipelines. Journal of Waterway, Port, Coastal, and Ocean Engineering, ASCE 132, 276–288.

Franco, L., Gerloni, M., Passoni, G., Zacconi, D., 1999. Wave forces on solid and perforated caisson breakwaters: comparison of field and laboratory measurements. In: In Coastal Engineering 1998. pp. 1945–1958.

Fredsøe, J., 2016. Pipeline-seabed interactions. Journal of Waterway, Port, Coastal, and Ocean Engineering 142 (6), 03116002.

Hasselmann, K., Barnett, T.P., Bouws, E., Carlson, H., Cartwright, D.E., Enke, K., Ewing, J.A., Gienapp, H., Hasselmann, D.E., Kruseman, P., Meerburg, A., Muller, P., Olbers, D.J., Richter, K., sell, W., Walden, H., 1973. Measurements of Wind-Wave Growth and Swell Decay during the Joint North Sea Wave Project (JONSWAP). Technical Report 8. Erganzungsheft zur Deutschen Hydrographischen Zeitschrift Reihe A.

Herbich, J.B., Schiller, R.E., Dunlap, W.A., Watanabe, R.K., 1984. Seafloor scour: Design guidelines for ocean-founded structures. Marcel Dekker.

Herbich, J. B., Schiller, R. E., Dunlap, W. A., Watanabe, R. K., 1984. Seafloor scour: Design guidelines for ocean-founded structures. New York: Marcel Dekker.

Higuera, P., Lara, J., Losada, I., 2013. Realistic wave generation and active wave absorption for vavier-stokes models: Application to openfoam. Coastal Engineeirng 71, 102–118.

Higuera, P., Lara, J. L., Losada, I. J., 2014a. Three-dimensional interaction of waves and porous coastal structures using openfoam. part i: Formulation and validation. Coastal Engineering 83, 243–258.

Higuera, P., Lara, J. L., Losada, I. J., 2014b. Three-dimensional interaction of waves and porous coastal structures using openfoam. part ii. application. Coastal Engineering 83, 259–270.

Ishihara, K., Towhata, I., 1983. Sand response to cyclic rotation of principal stress directions as induced by wave loads. Soils and Foundations 23 (4), 11–26.

Jeng, D.-S., 2001. Numerical modelling for wave-seabed-pipe interaction in a non-homogeneous porous seabed. Soil Dynamics and Earthquake Engineering 21 (8), 699–712.

Kazeminezhad, M. H., Bakhtiary, A. Y., Shahidi, A. E., Baas, J. H., 2012. Two-phase simulation of wave-induced tunnel scour beneath marine pipelines. Journal of Hydraulic Engineering 138 (6), 517–529.

Longuet-Higgins, M. S., 1957. The statistical analysis of a random, moving surface. Philios Trans Royal Society 249, 321–387.

Luan, M., Jeng, D.-S., Guo, Y., Yang, Q., 2008. Dynamic response of a porous seabed-pipeline interaction under wave loading: soil-pipeline contact effects and inertial effects. Computers and Geotechnics 35, 173–186.

Miyamoto, J., Sassa, S., Tsurugasaki, K., Sumida, H., 2020. Wave-induced liquefaction and floatation of a pipeline in a drum centrifuge. Journal of Waterway, Port, Coastal and Ocean Engineering, ASCE 146 (2), 04019039.

Pastor, M., Zienkiewicz, O. C., Chan, A. H. C., 1990. Generalized plasticity and the modeling of soil behaviour. International Journal for Numerical and Analytical Methods in Geomechanics 14, 151–190.

Sassa, S., Sekiguchi, H., 2001. Analysis of wave-induced liquefaction of sand beds. Géotechnique 51 (2), 115–126.

Sassa, S., Takayama, T., Mizutani, M., Tsujio, D., 2006. Field observations of the build-up and dissipation of residual pore water pressures in seabed sands under the passage of storm waves. Journal of Coastal Research SI39, 410–414.

Shi, Y. M., Gao, F. P., 2018. Lateral instability and tunnel erosion of a submarine pipeline: competition mechanism. Bulletin of Engineering Geology and the Environment 77, 1069–1080.

Sumer, B. M., 2014. Liquefaction around marine structures. World Scientific.

Sumer, B. M., C, C. T., Fredsøe, J., 2006. Liquefaction around pipelines under waves. Journal of Waterway, Port, Coastal, and Ocean Engineering, ASCE 132, 266–275.

Sumer, B. M., Fredsøe, J., 1990. Scour below pipelines in waves. Journal of Waterway, Port, Coastal and Ocean Engineering 116 (3), 307–323.

Sumer, B. M., Fredsøe, J., Christensen, S., Lind, M. L., 1999. Sinking/floatation of pipelines and other objects in liquefied soil under waves. Coastal Engineering 38, 53–90.

Teh, T. C., Palmer, A. C., Damgaard, J. S., 2003. Experimental study of marine pipelines on unstable and liquefied seabed. Coastal Engineering 50, 1–17.

Towhata, I., Ishihara, K., 1985. Undrained strength of sand undergoing cyclic rotation of principal stress axes. Soils and Foundations 25 (2), 135–147.

Ulker, M., Rahman, M. S., 2009. Response of saturated and nearly saturated porous media: Different formulations and their applicability. International Journal for Numerical and Analytical Methods in Geomechanics 33 (5), 633–664.

Wang, Z., Liu, P., Jeng, D.-S., Yang, Q., 2017a. Cyclic strength of sand under a nonstandard elliptical rotation stress path induced by wave loading. Journal of Hydrodynamics, Series B 29 (1), 89–95.

Wang, Z. T., Liu, P., Chan, A., Jin, D., 2017b. Principal stress rotation and cyclic shear strength for an elliptical rotation stress path. Marine Georesources & Geotechnology 35 (8), 1077–1085.

Yamamoto, T., Koning, H., Sellmeijer, H., Hijum, E. V., 1978. On the response of a poro-elastic bed to water waves. Journal of Fluid Mechanics 87 (1), 193–206.

Zhao, H., Liang, Z., Jeng, D.-S., Zhu, J., Guo, Z., Chen, W., 2018a. Numerical investigation of dynamic soil response around a submerged rubble mound breakwater. Ocean Engineering 156, 406–423.

Zhao, H. Y., Jeng, D.-S., 2016. Accumulated pore pressures around submarine pipeline buried in trench layer with partial backfills. Journal of Engineering Mechanics, ASCE 142 (7), 04016042.

Zhao, H.-Y., Jeng, D.-S., Guo, Z., Zhang, J.-S., 2014. Two dimensional model for pore pressure accumulations in the vicinity of a buried pipeline. Journal of Offshore Mechanics and Arctic Engineering, ASME 136(4), 042001.

Zhao, H. Y., Zhu, J. F., Zheng, J. H., Zhang, J. S., 2020. Numerical modelling of the fluid-seabed-structure interactions considering the impact of principal stress axes rotations. Soil Dynamics and Earthquake Engineering 136, 106242.

Zhao, K., Xiong, H., Chen, G. X., Zhao, D. F., Chen, W. Y., Du, X. L., 2018b. Wave-induced dynamics of marine pipelines in liquefiable seabed. Coastal Engineering 140, 100–113.

Zhu, J. F., Zhao, H. Y., Jeng, D.-S., 2019. Effects of principal stress rotation on wave-induced soil response in a poro-elastoplastic sandy seabed. Acta Geotechnica 14 (6), 1717–1739.